

# Hydrodynamic Simulations of Asymmetric Propeller Structures in Saturn’s Rings

M. SEILER,<sup>1</sup> M. SEISS,<sup>1</sup> H. HOFFMANN,<sup>1</sup> AND F. SPAHN<sup>1</sup>

<sup>1</sup>*Theoretical Physics Group, Institute of Physics and Astronomy, University of Potsdam, Germany*

Submitted to ApJS

## ABSTRACT

The observation of the non-Keplerian behavior of propeller structures in Saturn’s outer A ring (Tiscareno et al. 2010; Seiler et al. 2017; Spahn et al. 2018) raises the question, how the propeller responds to the wandering of the central embedded moonlet. Here, we study numerically how the induced propeller is changing for a librating moonlet. It turns out, that the libration of the moonlet induces an asymmetry in the structural imprint of the propeller, where the asymmetry is depending on the moonlet’s libration period and amplitude. Further, we study the dependence of the asymmetry on the libration period and amplitude for a moonlet with 400 m Hill radius, which is located in the outer A ring. In this way, we are able to apply our findings to the largest found propeller structures – such as Blériot – which are expected to be of similar size. For Blériot, we can conclude that, supposed the moonlet is librating with the largest observed period of 11.1 years and an azimuthal amplitude of about 1845 km (Seiler et al. 2017; Spahn et al. 2018), a small asymmetry should be measurable but depends on the moonlet’s libration phase at the observation time. The excess motions of the other giant propellers – such as Santos Dumont and Earhart – have similar amplitudes as Blériot and thus might allow the observation of larger asymmetries due to their smaller azimuthal extent. This would permit to scan the whole gap structure for asymmetries.

Although the librational model of the moonlet is a simplification, our results are a first step towards the development of a consistent model for the description of the formation of asymmetric propellers caused by a freely moving moonlet.

*Keywords:* hydrodynamics — methods: numerical — methods: data analysis — planets and satellites: dynamical evolution and stability — planets and satellites: rings — planets and satellites: individual(Saturn)

## 1. INTRODUCTION

Planetary rings are one of the most beautiful structures in our solar system, which are mainly

composed of differently sized icy particles. The dense main rings of Saturn are composed of particles ranging from centimeters to a few meters (Cuzzi et al. 2018) and beside this ensemble of particles, even larger boulders (called *moonlets*) are orbiting within the ring environment. By their strong gravitational interaction with the

Corresponding author: M. Seiler  
[miseiler@uni-potsdam.de](mailto:miseiler@uni-potsdam.de)

surrounding ring material, these objects try to sweep free a gap around their orbits. Due to the different angular speeds of the ring material for varying semi-major axis the gap appears inside and outside the moonlet’s mean radial position with a slight radial shift. Therefore, the inner gap – due to the higher angular speed of the ring material – overtakes the embedded moonlet while the outer one falls behind. Viscous diffusion of the ring material counteracts this gravitational scattering process and thus results in a closing of the opened gap with growing azimuthal distance to the embedded moonlet (Spahn and Sremčević 2000; Sremčević et al. 2002; Seiß et al. 2005; Hoffmann et al. 2015). For moonlets larger than a critical radius, its gravity compensates the viscous diffusion along the whole circumference of the orbit and thus the gap is kept open. For smaller moonlet radii, the gravity of the moonlet does not suffice to compensate the viscous diffusion and therefore the gap closes. As a result, two partial gaps inside and outside the orbit of the moonlet decorated with wakes remain and resemble an S-shaped, two-bladed *propeller*. Those propellers act as structural insignia to detect the embedded moonlet in the dense rings.

After the postulation of their existence in Saturn’s ring to explain optical depth variations in the Voyager data (Henon 1981; Lissauer et al. 1981), the cameras onboard the spacecraft Cassini finally revealed their presence within the dense rings of Saturn (Tiscareno et al. 2006; Spahn and Schmidt 2006; Sremčević et al. 2007; Tiscareno et al. 2008). Meanwhile, different populations of propeller structures inside Saturn’s A ring have been identified in the images. Between 127 000 and 132 000 km from Saturn’s center three *propeller belts* have been observed, which contain several thousand propellers, all being generated by moonlets of radii  $\lesssim 0.15$  km (Tiscareno et al. 2008). Further outwards, between the Encke and Keeler gap, about 37

larger propellers being created by moonlets with radii between  $\sim 0.15$  km and  $\lesssim 1.0$  km have been found (Tiscareno et al. 2010). Due to their relatively large size, 11 of these *giant-propellers* were able to be identified in different subsequent images, allowing the reconstruction of their orbital motion. The analysis of their orbital evolution revealed a longitudinal deviation from their expected Keplerian location – called *excess motion* (Tiscareno et al. 2010; Spahn et al. 2018).

The largest propeller structure is called Blériot and is created by a moonlet of about 400 m in Hill radius (Hoffmann et al. 2016; Seiß et al. 2017). Its excess motion can be reconstructed by a superposition of three sinusoidal harmonics with periods of 11.1, 3.7 and 2.2 years and amplitudes of 1845, 152 and 58 km with a standard deviation of about 17 km of the remaining residual (Seiler et al. 2017; Spahn et al. 2018). Blériot’s excess motion resembles the typical librational motion of a resonantly perturbed moon (Goldreich 1965; Goldreich and Rappaport 2003a,b; Spitale et al. 2006; Cooper et al. 2015) and thus supports the hypothesis, that this excess motion might result from a resonant or near-resonant driving by one or several of the outer satellites. In numeric simulations <sup>1</sup> it has been shown, that the collective perturbation by the outer satellites Prometheus, Pandora and Mimas is able to induce correct libration frequencies to explain the three mode fit, but the induced libration amplitudes are by far too small to explain the observations (Seiler et al. 2017).

Alternatively, a stochastic migration of the embedded moonlet due to collisions or density fluctuations in the rings has been proposed as well (Crida et al. 2010; Rein and Papaloizou 2010; Pan and Chiang 2010, 2012; Pan

<sup>1</sup> In these simulations a test moonlet, which has been placed on the expected orbital position of Blériot, has been driven gravitationally by Saturn and 15 of its larger moons.

et al. 2012; Bromley and Kenyon 2013; Tiscareno 2013). The most promising results have been obtained by Rein and Papaloizou (2010), who considered a random walk in the semi-major axis of the moonlet, and in N-Body simulations Pan et al. (2012) have been able to generate an amplitude in the moonlet’s excess motion of about 300 km over a time span of 4 years. Nevertheless, their resulting amplitude is also too small.

In order to solve this amplitude problem Seiler et al. (2017) suggested a propeller-moonlet interaction model, where the usually assumed point-symmetry of the propeller structure is broken by a slight displacement of the central moonlet. This breaking of the point-symmetry causes a restoring force to the moonlet, resulting in a harmonic oscillation in the moonlet’s mean longitude. The libration depends on the physical parameters of the propeller and the surrounding ring material. This oscillating system has its own eigenfrequency so that for an external resonant driving with a frequency, which is sufficiently close to the eigenfrequency of the propeller-moonlet oscillator, an originally small libration mode can be amplified by several orders of magnitude.

However, the suggested propeller-moonlet interaction model is oversimplifying the physical problem in the aspect, that it reduces the gap structures to two radially separated rectangular shaped boxes with fixed azimuthal end points, where the beginning of the gap follows the moonlet motion. Further, the surface mass density inside these boxes is assumed to be constant. In reality, the gap structure has an azimuthal extent of up to several thousand kilometers and the surface mass density within the gap structure is rather a decay than constant. Due to the radial separation of the gaps from the moonlet, the perturbation caused by the moonlet’s motion first needs time to be transported along the gap structure, given by the Kepler

shear. Thus, the perturbation by the moonlet’s motion only arrives at the gap ends after a certain delay time (hereafter called  $T_{gap}$ ), while the beginning of the gap more or less follows the moonlet motion instantaneously. For Blériot this delay time would be about  $T_{gap} \approx 0.5$  years considering a gap length of 6500 km, respectively (Seiler et al. 2017). As a consequence of the moonlet’s wandering and the retardation in the reaction of the gap ends, the gap structures are expected to become asymmetric. Here, this expectation is tested for a given moonlet libration to answer the question, whether such an asymmetry might be detectable in the Cassini ISS images. Therefore, we search the simulated gap structures for properties which allow a direct measurement of the asymmetry. In addition, we will study the dependence of the asymmetry on the libration amplitude and period.

The plan of this paper is as follows: First, we give an overview of our hydrodynamic simulation code and how we model the moonlet libration (see Section 2). Afterwards, we present the results of our simulations and show, how the appearance of the propeller and the different properties of the gap structures change with the libration of the moonlet. For this purpose, we directly compare our results to simulations of a symmetric propeller structure (see Section 3). The propeller-moonlet interaction model predicts, that the restoring force by the gap-asymmetry follows the moonlet motion. This fact will be checked against our simulation data (see Section 4). As a next step, we study the dependence of the asymmetry on the libration period and amplitude and test, under which conditions the asymmetry becomes detectable (see Section 5). On the basis of our analysis, we will apply our findings to the propeller Blériot in Section 5.3. In the end of this paper, we conclude and discuss our findings (see Section 6).

## 2. HYDRODYNAMIC SIMULATION

Our hydrodynamic simulation routine bases on the code, developed by [Seiß et al. \(2017\)](#). This integration routine will be modified so that the moonlet can librate around its mean orbital position within the simulation grid.

We consider a moonlet embedded in the granular environment of Saturn's rings with surface mass density  $\Sigma$ . The evolution of the surface mass density is described by the continuity equation

$$\partial_t \Sigma + \nabla \cdot \Sigma \mathbf{v} = 0 \quad (1)$$

and the momentum balance is quantified by the Navier Stokes equation

$$\partial_t \Sigma \mathbf{v} + \nabla \cdot (\Sigma \mathbf{v} \circ \mathbf{v}) = -\Sigma \nabla \cdot (\Phi_p + \Phi_m) + \mathbf{f}_i - \nabla \cdot \hat{\mathbf{P}}. \quad (2)$$

Both equations above are presented in the flux conserved form, where the tensor product is denoted by the  $\circ$  symbol. The symbol  $\partial_t = \partial/\partial t$  denotes the partial time derivative. The gravitational potentials of the central planet and the moonlet are described by  $\Phi_p$  and  $\Phi_m$ . Further, we choose our simulation's coordinate system to co-rotate with the moonlet's mean orbital frequency  $\Omega = \sqrt{GM_p/r_0^3}$ , where  $G$  and  $M_p$  denote the gravitational constant and the mass of the central planet, and to be centered at the moonlet's mean radial position  $r_0$ . Here, we neglect the oblateness of Saturn <sup>1</sup>.

In comparison to their radial and longitudinal extent (several hundred thousand kilometers) the vertical dimension ( $\lesssim 100$  m) of Saturn's rings is tiny. Thus, equations 1 and 2 can

<sup>1</sup> Including the oblateness of Saturn would result in slightly different orbital frequencies and in a precession of the ascending node and the pericenter, which will not have a significant impact on the results, since we are only considering a small ring area in the close vicinity of the moonlet.

be reduced to a two-dimensional problem using vertically integrated quantities ([Spahn et al. 2018](#)). Additionally, the moonlets in the outer A ring are expected to evolve on nearly circular orbits in the equatorial plane of Saturn.

In comparison to the spatial extent of the rings the propellers are tiny. As a consequence, only a small ring area, centered around the moonlet's orbital position needs to be considered for our simulations. Therefore, the acting forces in the vicinity of the moonlet can be linearized and described by the Hill problem ([Hill 1878](#)). Here, we choose  $x$  to represent the radial distance from the moonlet and  $y$  stands for the azimuthal direction. As a result, the gravitational potential of the central moonlet is given by

$$\Phi_m = -\frac{GM_m}{\sqrt{x^2 + y^2 + \epsilon^2}}, \quad (3)$$

with  $\epsilon$  the smoothing radius which limits the gravitational potential in the close vicinity of the moonlet's center. Here, we choose  $\epsilon = 0.2$  h. The mass of the moonlet  $M_m$  is defined by its Hill radius

$$h = a_0 \sqrt{\frac{M_m}{3M_p}}, \quad (4)$$

where  $a_0$  denotes the semi-major axis of the moonlet's mean orbit.

We treat the granular ensemble forming dense rings as a usual (linear) fluid. Thus, the pressure tensor  $\hat{\mathbf{P}}$  can be described with the Newtonian ansatz as

$$P_{ij} = p \delta_{ij} - \Sigma \nu \left( \frac{\partial v_i}{\partial x_j} + \frac{\partial v_j}{\partial x_i} \right) + \Sigma \left( \frac{2}{3} \nu - \xi \right) \nabla \cdot \mathbf{v} \delta_{ij} \quad (5)$$

where  $p$ ,  $\nu$  and  $\xi$  denote the scalar pressure, the kinematic shear and the bulk viscosities, respectively. The dependence of the pressure and the viscosities on the local density can be described by the power laws ([Spahn et al. 2000](#))

$$p = p_0 \left( \frac{\Sigma}{\Sigma_0} \right)^\alpha \quad (6)$$

$$\nu = \nu_0 \left( \frac{\Sigma}{\Sigma_0} \right)^\beta \quad (7)$$

Additionally, we set the ratio between shear and bulk viscosity constant

$$\xi = \frac{\xi_0}{\nu_0} \cdot \nu \quad (8)$$

In the simplest case, the unperturbed pressure is given by the ideal gas relation  $p_0 = \Sigma_0 c_0^2$  at equilibrium, where  $c_0$  denotes the dispersion velocity. In our simulation scheme, we use an isothermal model and therefore the dispersion velocity  $c_0$  and the related granular temperature  $T = c_0^2/3$  are constant.

### 2.1. Methods

The simulation area is a rectangular cut out of the ring environment of dimensions  $(x_{\min}, x_{\max})$  and  $(y_{\min}, y_{\max})$ , which is centered around the mean orbital position of the moonlet. This box is divided into  $N_x \times N_y$  equal-sized cells. The complete set of equations is integrated until a steady state is established. The advection term is solved with the second-order scheme with 'MinMod' flux limiter (LeVeque 2002) in order to better conserve the wake crests. The influence of pressure and viscous transport is solved with an explicit scheme. At the borders of the calculation regions, the boundary conditions are chosen such, that the perturbations can flow out of the box freely, while the inflow is unperturbed. This is especially important at the azimuthal boundaries, where due to Kepler shear the material is flowing into the box at  $x < 0, y = y_{\min}$  and  $x > 0, y = y_{\max}$  and flowing out at  $x < 0, y = y_{\max}$  and  $x > 0, y = y_{\min}$ . The influence of the moonlet is established mainly by its gravity.

A more detailed overview of the implementation of the integration routine and the used

Parameter	Value
$h$	400 m
$\Omega$	$1.3 \times 10^{-3} \text{ s}^{-1}$
$\nu_0$	$300 \text{ cm}^2 \text{ s}^{-1}$
$c_0$	$0.5 \text{ cm s}^{-1}$

**Table 1.** Simulation parameters for the hydrodynamic simulation. Those parameters are used for the scaling within the integration routine.

numerical methods is given in Section 3 in Seiß et al. (2017).

The simulation scheme uses following scaled values:  $x \rightarrow x/h$ ,  $y \rightarrow y/h$ ,  $t \rightarrow \Omega t \sim t/T$  and  $\Sigma \rightarrow \Sigma/\Sigma_0$ .

Here, we will focus on the asymmetry formation for the giant trans-Encke propellers. For this reason, we will consider a Blériot-sized moonlet with 400 m Hill radius (Hoffmann et al. 2016; Seiß et al. 2017), allowing us to predict the asymmetry of its propeller. Therefore, we will simulate the moonlet at a radial location close to its observed orbital position and we will adopt the viscosity accordingly (Seiß et al. 2017). The set of used parameters and their values – if nowhere else mentioned – are given in Table 1.

The scaled viscosity and sound speed are calculated according to the moonlet size

$$\tilde{\nu} = \frac{\nu_0}{h^2 \Omega} \quad \text{and} \quad (9)$$

$$\tilde{c} = \frac{c_0}{h \Omega} \quad (10)$$

Their value and further parameters used for the simulation are given in Table 2.

### 2.2. Modeling the Moonlet Motion

The observed harmonic excess motion of Blériot requires a periodic azimuthal motion of the propeller structure. In the easiest way, this can be achieved by a libration of the central moonlet. Setting the moonlet on a librational motion around its mean orbital position further allows to directly test the assumptions of

Parameter	Value
$\tilde{\nu}$	$1.441 \times 10^{-3}$
$\tilde{c}$	$4.811 \times 10^{-2}$
$\alpha$	1
$\beta$	2
$\tilde{\xi}$	$7 \tilde{\nu}$
$x_{\min}$	-10 h
$x_{\max}$	10 h
$y_{\min}$	-800 h
$y_{\max}$	800 h
$N_x$	400
$N_y$	6400

**Table 2.** Further simulation parameters used for the hydrodynamic simulation.

the propeller-moonlet interaction model (Seiler et al. 2017).

The moonlet will be set on a librational motion with amplitude  $x_{m,0}$  and period  $T_m$  given by

$$x_m = x_{m,0} \cos\left(\frac{2\pi}{T_m}t\right) \text{ and} \quad (11)$$

$$y_m = -\frac{3}{2}x_{m,0}T_m \sin\left(\frac{2\pi}{T_m}t\right). \quad (12)$$

Note, that the above presented equations for the moonlet motion are already given in the scaled form, where the time  $t$  and the libration period  $T_m$  are given in number of orbits and the directions  $x_m$  and  $y_m$  are given in Hill radii. The moonlet’s azimuthal amplitude is motivated by the proportionality of  $dn/dt \propto da/dt$  and thus it is set by the Kepler shear.

The advantage of the librational moonlet motion lies in the fact, that it covers both, libration and migration. The resulting asymmetry for a linearly migrating moonlet can be studied considering only part of the moonlet libration. In this context, the relative velocity of the perturbed moonlet motion to its unperturbed orbit – which depends on the amplitude  $x_{m,0}$  and

period  $T_m$  – will also set the drift rate of the moonlet.

### 3. VISUALIZATION OF THE ASYMMETRY

For the presentation of our simulation results, we will define and analyze different characteristics of the propeller shape and directly compare the results for a symmetric and asymmetric propeller. In this way, we show, how the asymmetry of the propeller can be characterized. Our results have been obtained for a moonlet with 400 m Hill radius. For the asymmetric propeller – if nowhere else mentioned – the moonlet has been forced to around its mean orbital position with a radial amplitude of  $x_{m,0} = 0.5$  h and period of  $T_m = 80$  orbital periods.

#### 3.1. Density Profile

The typical imprint of an unperturbed propeller structure, where the moonlet (represented by the star symbol) is not librating, is shown in the top panel of Figure 1. A clear symmetry can be seen. The grey scale color code illustrates the surface mass density, where darker color corresponds to regions of depleted density, while brighter color represents denser regions. The  $x$  and  $y$  directions in the presented plots denote the radial and azimuthal distances to the mean orbital position of the moonlet. For a better visualization, the presented area around the propeller is reduced radially and azimuthally to  $\Delta x = \pm 6$  h and  $\Delta y = \pm 600$  h. Note, that the moonlet’s mean orbital motion is from left to right.

Fresh inflowing material (moving from left to right) passing by the moonlet from the inside at  $\Delta x < 0$ , are the more deflected to the moonlet the closer they pass it radially. The deflection for the particles passing by outside at  $\Delta x > 0$  the moonlet moving from right to left occur vice versa. For larger radial distances, this deflection decreases as  $|\Delta x|^{-2}$ . This induces a coherent motion of the ring material and thus results in the formation of wakes. The location

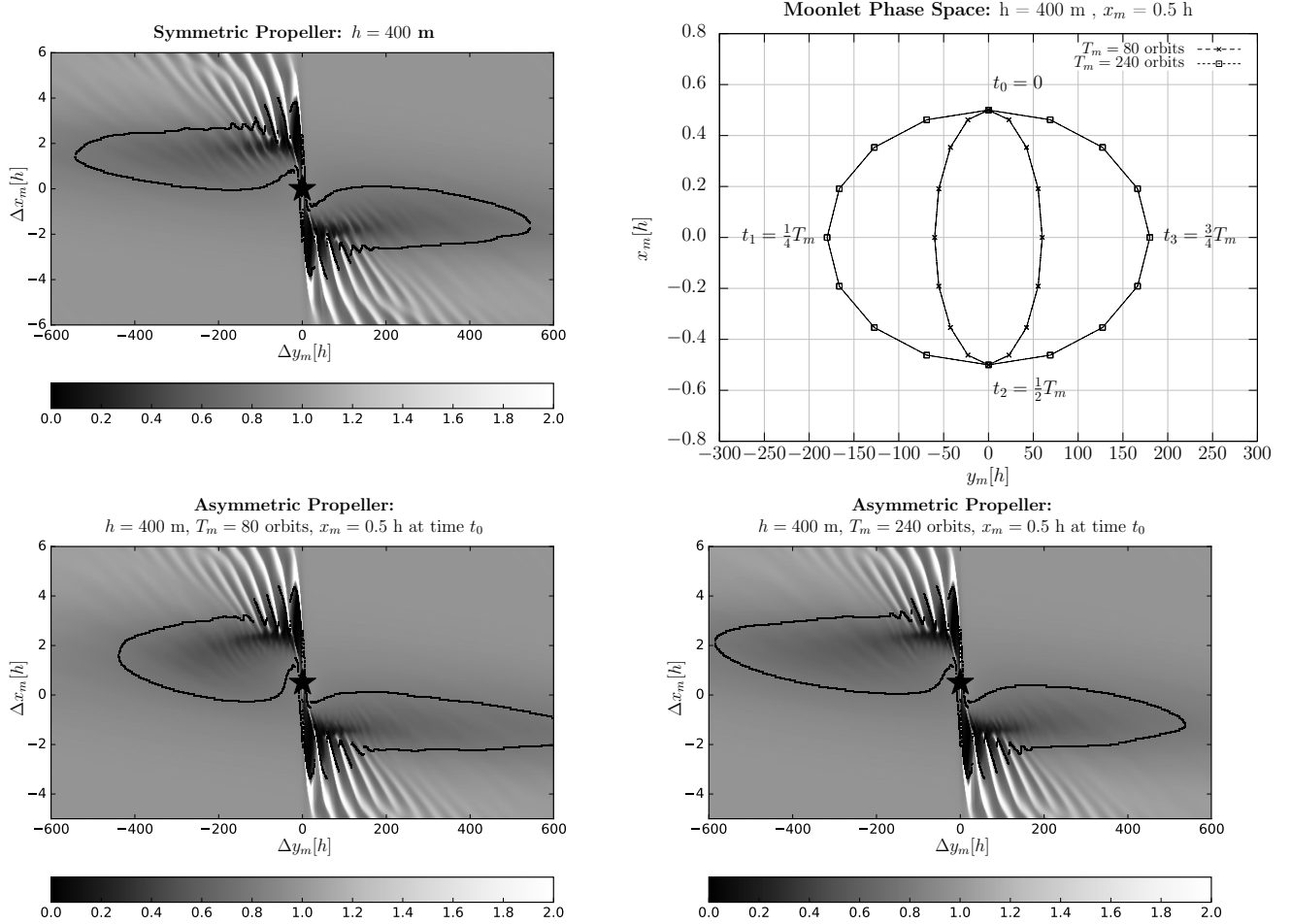


**Figure 1.** Comparison of a symmetric propeller (top left) and two examples for an asymmetric propeller (bottom panels). The two asymmetric examples show the propeller for a librating moonlet at the same libration phase, but for different libration periods (see top right panel). In the bottom left panel the moonlet is librating with  $T_m = T_{gap}$ , while in the right one the period is  $T_m = 3 \times T_{gap}$ . In all panels, the origin of the coordinate system is centered to the mean orbital position of the moonlet. The moonlet's actual position is given by the star symbol. In all cases the moonlet's Hill radius is  $h = 400$  m and its libration amplitude was set to  $x_{m,0} = 0.5$  h. The black lines denote the density profile at 80% gap relaxation.

of the moonlet within the simulation grid, which is centered to its mean orbital location, is illustrated by the star symbol. Further, the black line marks the propeller surface mass density level at 80% of gap closing ( $\Sigma/\Sigma_0 = 0.8$ ). At this level of surface mass density, a clear symmetry can be seen when comparing the inner and outer gap region, where the gap lengths are about 540 h and the maximum gap widths are about 2 h, respectively.

This symmetry is broken in the bottom panels of Figure 1, where snapshots of the induced propeller structures for a librating moonlet are given. The azimuthal and radial scales are chosen exactly in the same way as for the unperturbed case. The level of  $\Sigma/\Sigma_0 = 0.8$  is emphasized by the black line, where a clear difference in the gap lengths and even in the gap widths is obvious. The two bottom panels in Figure 1 show the propeller structure at the same libration phase of the moonlet but for dif-

ferent libration periods. In the left panel the moonlet’s libration period has the value  $T_m = 80$  orbits, while its value is  $T_m = 240$  orbits in the right one. The iso-density level  $\Sigma/\Sigma_0 = 0.8$  level is suitable to illustrate the asymmetry: The bottom left panel (shorter  $T_m$ ) shows a length ratio between the outer and inner gap of  $450\text{ h}/650\text{ h} \approx 0.7$  and in the other case (bottom right panel,  $T_m = 3 \times T_{gap}$  this ratio takes  $600\text{ h}/550\text{ h} \approx 1.09$ , which makes the propeller gaps look more symmetric. For the gap width at  $\Delta = \pm 150\text{ h}$  the width ratio between the outer and inner gap has a value of  $3\text{ h}/2\text{ h} = 1.5$  for the bottom left panel, while for the bottom right panel this ratio is  $3\text{ h}/2.5\text{ h} = 1.2$ .

For the used dimension of the simulation box (see Table 2) a steady state is already reached after 80 orbits, respectively. This equals the time the fresh ring material at  $\Delta x = \pm 1\text{ h}$  needs to drift to the moonlet. For the moonlet used with Hill radius of  $h = 400\text{ m}$  the azimuthal extent is of similar size (about 600 h at  $\Sigma/\Sigma_0 = 0.8$  as seen in the top panel of Figure 1). In this case, the perturbation by the moonlet motion would take about 63 orbits to reach the end of the gaps. Therefore, the two bottom panels of Figure 1 show the induced propeller structure for  $T_m \approx T_{gap}$  (left) and for  $T_m \approx 3 \times T_{gap}$  (right). It has to be noted, that the timescales involved depend on the mass (size) of the moonlet.

Due to the libration of the embedded moonlet, the shape of the propeller is changing all the time. Thus, at different phases of the moonlet’s libration the propeller structure looks different resulting in different gap lengths and gap depths, as presented in Figure 2. Here, the four center and bottom panels show the propeller shape for half a libration period at times  $t = 210, 220, 230$  and  $240$  orbits, while the top panel illustrates the actual position of the moonlet at those times. Note, that the moonlet libration is counter clockwise. The

propeller shape for the other half of the libration period would look similar but mirrored due to the Kepler shear. The snapshots at 220 orbits and 240 orbits show the moonlet at  $(x_m(t = 220\text{ orbits}) = 0\text{ h}, y_m(t = 220\text{ orbits}) = 60\text{ h})$  and  $(x_m(t = 240\text{ orbits}) = 0.5\text{ h}, y_m(t = 240\text{ orbits}) = 0\text{ h})$ . The strongest asymmetry of the propeller can be observed for the moonlet at its radial amplitude (see snapshot at  $t = 220$  orbits in Figure 2).

A more detailed analysis of the gap structures will be presented in the following sections.

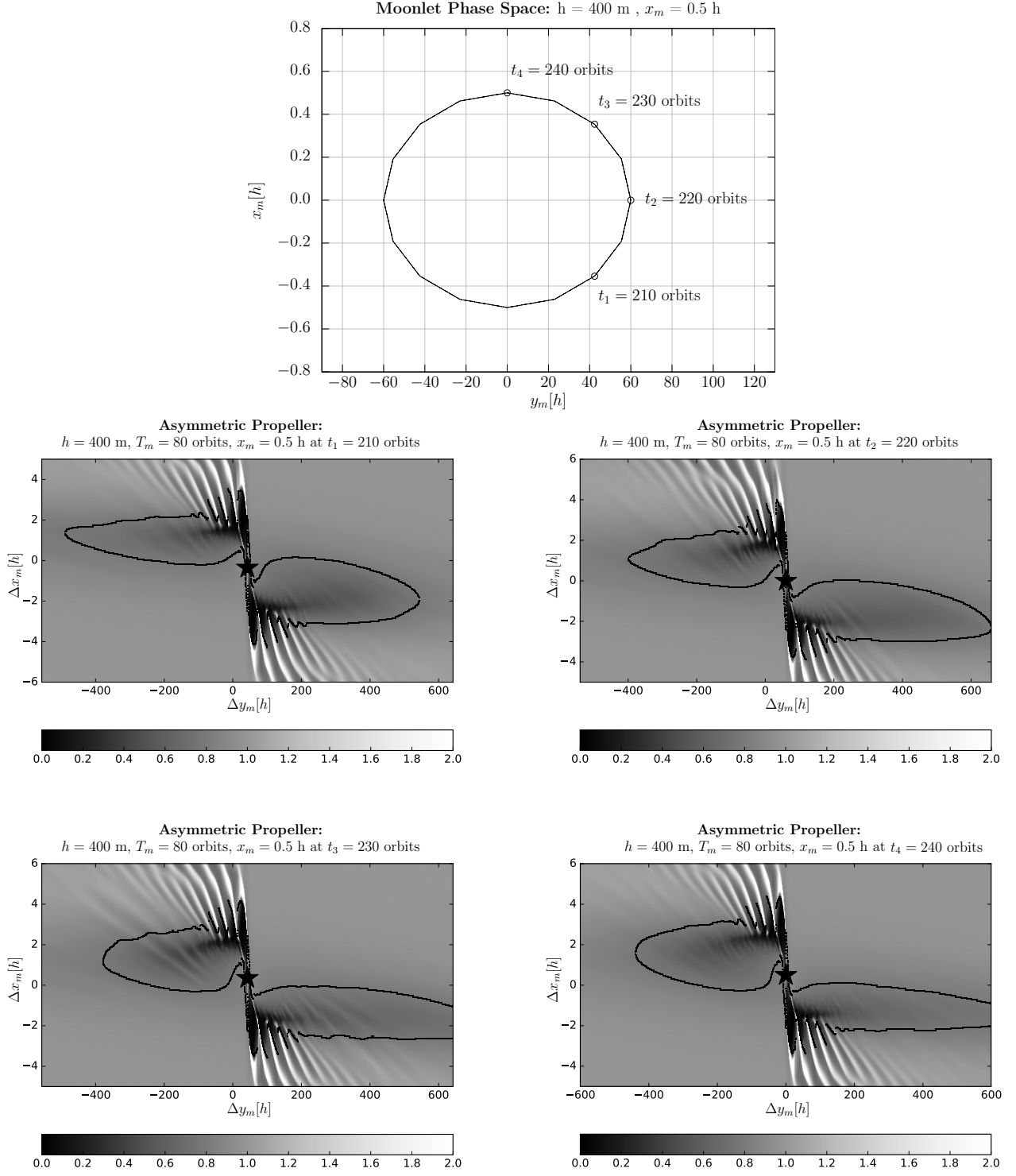
### 3.2. Radial Gap Profile

Figure 2 illustrates the evolution of the asymmetry of a propeller caused by a librating moonlet. The grey-level density representations correspond to certain times  $t = (210, 220, 230, 240)$  orbits, which represent four different phases (phase angles) of the moonlet libration.

We will analyze and compare the radial gap profiles of a symmetric and asymmetric propeller at different azimuthal distances to the moonlet which demonstrate the changes in the gap structures due to the moonlet motion. The minimum of the surface mass density defines the gap depth and its radial position gives the gap position. At the fixed surface density level  $\Sigma/\Sigma_0 = 0.8$  we estimate the gap width, permitting the comparison of the inner and outer gap in this way.

First, we reduce the noise of the simulation data – especially in the wake region close to the moonlet – by performing moving box averaging for the radial gap profiles, where the radial box length is set close to the wake wavelength of about  $\Delta x = 0.5\text{ h}$ . The resulting smoothed radial density profiles of the inner and outer gap at azimuthal distances to the moonlet of  $\Delta y = |y - y_m| = 10, 200$  and  $600\text{ h}$  are shown in Figure 3. Note, that for the bottom panels in Figure 3 we use a moonlet-centered coordinate system ( $\Delta x = x - x_m(t)$  and  $\Delta y = y - y_m(t)$ ) where we subtract of the moonlet’s actual posi-





**Figure 2.** Evolution of the propeller asymmetry for half a moonlet period. Top panel: Phase space representation of the moonlet libration highlighting the four different libration phase angles shown in the center and bottom panels. The moonlet of size  $h = 400$  m librates with a period of  $T_m = 80$  orbits and amplitude of  $x_{m,0} = 0.5$  h. The snapshots (center and bottom panels) show the moonlet (star symbol) at different libration phases at times  $t_1 = 210$  orbits (middle left),  $t_2 = 220$  orbits (middle right),  $t_3 = 230$  orbits (bottom left), and  $t_4 = 240$  orbits (bottom right).

tion for better comparison to the unperturbed moonlet profiles. The solid and dashed curves denote the inner and outer gap profiles. Note, that we mirrored the inner gap's profile at the origin to compare both gap profiles in a better way.

The top panel of Figure 3 shows the radial profile for the symmetric propeller. Here, the gap locations of the inner and outer gap match at all azimuthal distances. Further, the gap relaxes azimuthally as theoretically predicted, i.e. the gap-depth decreases for increasing azimuthal distance to the moonlet.

In the bottom panels the asymmetric gap profiles are illustrated at the two snapshots  $T = 220$  orbits and  $T = 240$  orbits from Figure 2. Here, the moonlet is presented at its azimuthal (left) and radial (right) libration amplitude. While in the left panel the gap profiles look much alike, but are shifted radially with increasing azimuth, their depths and widths differ significantly in the right panel. Note, how the beginning of the gaps (compare  $\Delta y = 10$  h) stays unaffected by the moonlet libration and follows the moonlet motion instantaneously in both panels.

### 3.2.1. Gap Positions

The changes in the gap minima locations caused by the moonlet libration can be better illustrated by considering their time-evolution for a fixed azimuth, as shown in Figure 4, where the evolution of the gap minima locations at  $\Delta y = |y - y_m| = 10, 200$  and  $600$  h is presented.

For the symmetric propeller the radial gap positions for different azimuths lay on top of each other, where the mean radial gap position  $\langle x_{gap} \rangle \approx \pm 2.83$  h (at  $\Delta y = \pm 10$  h) decreases to  $\langle x_{gap} \rangle \approx 1.6$  h (for  $\Delta y = \pm 200$  and  $\pm 600$  h) for larger azimuthal distances.

Figure 4 shows the time-evolution of the gap minima location for the symmetric (left panel) and the asymmetric (right panel) propeller. For the asymmetric case, it is visible, how the lo-

cations of the gap minima clearly follow the moonlet libration (black dotted line). Further, the radial amplitude of the gap location slightly increases for larger azimuthal distance to the moonlet. For the symmetric case, the radial gap locations stay constant over time.

While the ring material in the close vicinity to the moonlet almost immediately feels the change in the moonlet's motion (compare the the black solid and dashed lines in Figure 4), the perturbation by the motion of the moonlet first needs to be transported through the ring environment to larger azimuthal distances

$$\Delta y = -\frac{3}{2}\Omega_m t \Delta x \quad (13)$$

set by the Kepler shear. Thus, when the moonlet reaches its radial libration amplitude of  $0.5$  h at  $T = 80$  orbits the gap minima at  $\Delta y = 200$  h and  $\Delta y = 600$  h are following the moonlet motion after about 26 orbits and 80 orbits, respectively. This agrees with the delay found in Figure 4.

### 3.2.2. Radial Gap Separation

Although the radial locations of the gap minima change over time and can differ by more than 1 h (compare the solid and dashed red lines in Figure 4), their separation stays almost constant over time (see Figure 5). The evolution of the radial gap separation is presented at azimuthal distances to the moonlet of  $\Delta y = |y - y_m| = 10, 200$  and  $600$  h, where the dashed and solid lines denote the symmetric and asymmetric gap separation, respectively. With increasing azimuth the scattering of the radial gap separation becomes larger (about 1 h at  $\Delta y = \pm 600$  h and  $0.5$  h at  $\Delta y = \pm 200$  h). This is illustrated in the left panel of Figure 5, where a comparison of the gap separation for the symmetric propeller structure (red solid line) along the azimuth is compared against the asymmetric one (black lines) for three different snapshots. Comparing all the curves, one rec-

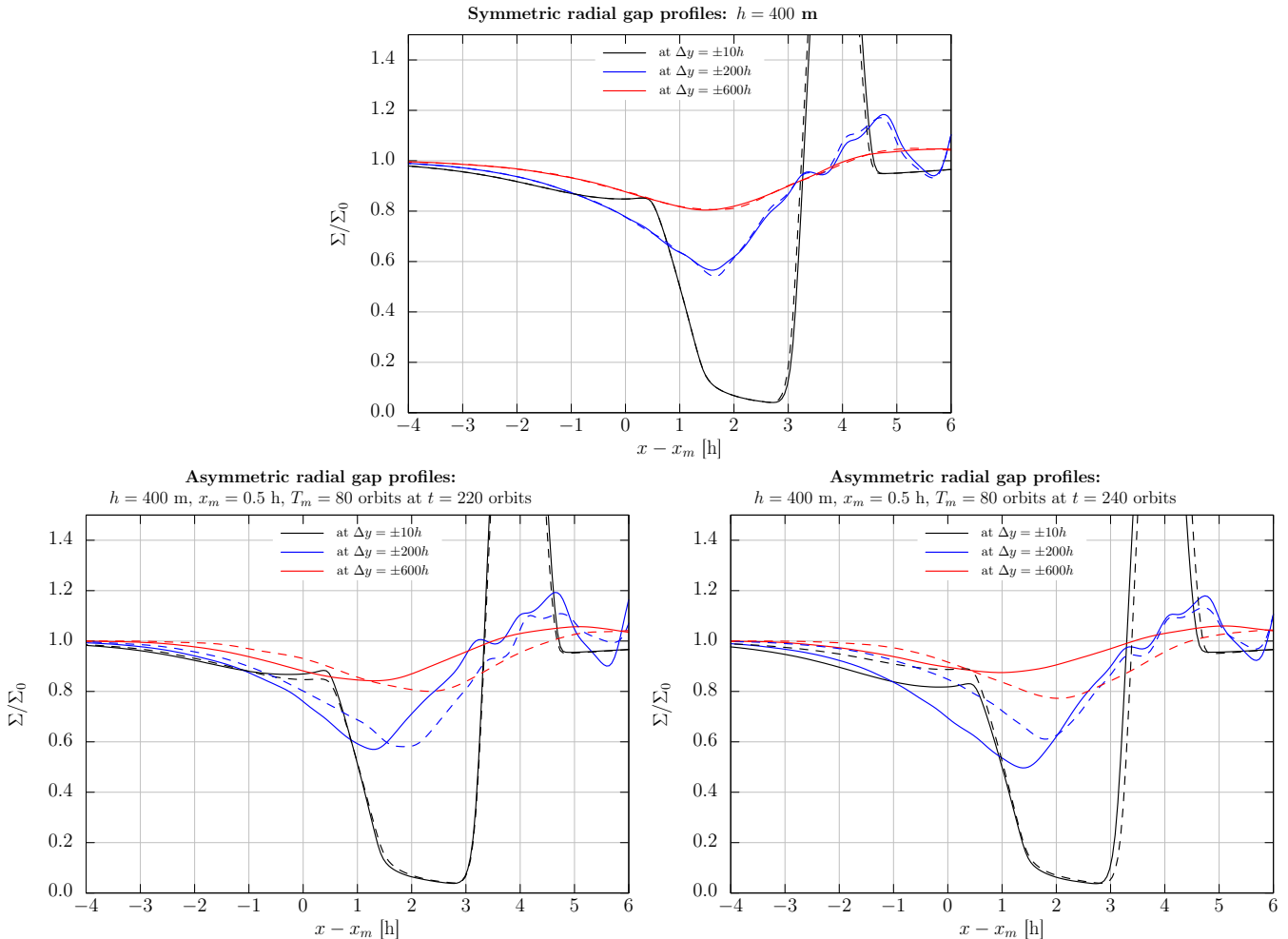


**Figure 3.** Radial gap profiles for a symmetric (Top) and asymmetric propeller structure (Bottom Left and Right) at different azimuthal distances to the moonlet of  $\Delta y = \pm 10h$  (black),  $\pm 200h$  (blue),  $\pm 600h$  (red). The dashed and solid lines denote the outer and inner gap profile. The inner gap’s profile has been mirrored at the moonlet position for better comparison. For the asymmetric propeller (Bottom panels) the radial gap profile is given at two different libration phases of the moonlet. Here, the moonlet size has been set to  $h = 400$  m and the libration period and amplitude have been set to 80 orbits and 0.5 h. For better comparison, the moonlet’s current position has been subtracted of in the case of the asymmetric propeller.

ognizes, that up to a critical azimuth of about 250 h the variations of the radial gap separation for the asymmetric gaps are negligible and thus it almost matches the symmetric gap structure.

For larger azimuthal distances to the moonlet, the retardation effect gets more dominant resulting in larger variations of the radial gap separation along the azimuth with time. This allows to detect the perturbation by the moonlet motion which gets visible as a wavy structure along the azimuth. Further, comparing the dif-

ferent snapshots at times  $T = 200$  orbits and  $T = 220$  orbits the propagation of the perturbation along the azimuth can be observed. On average, the gap separation still follows the azimuthal behavior of the unperturbed gap separation.

### 3.2.3. Gap Width

The grey-level density plots in Figure 1 and the radial profiles presented in Figure 3 have demonstrated, that the gap width is influenced by the motion of the moonlet. We study the

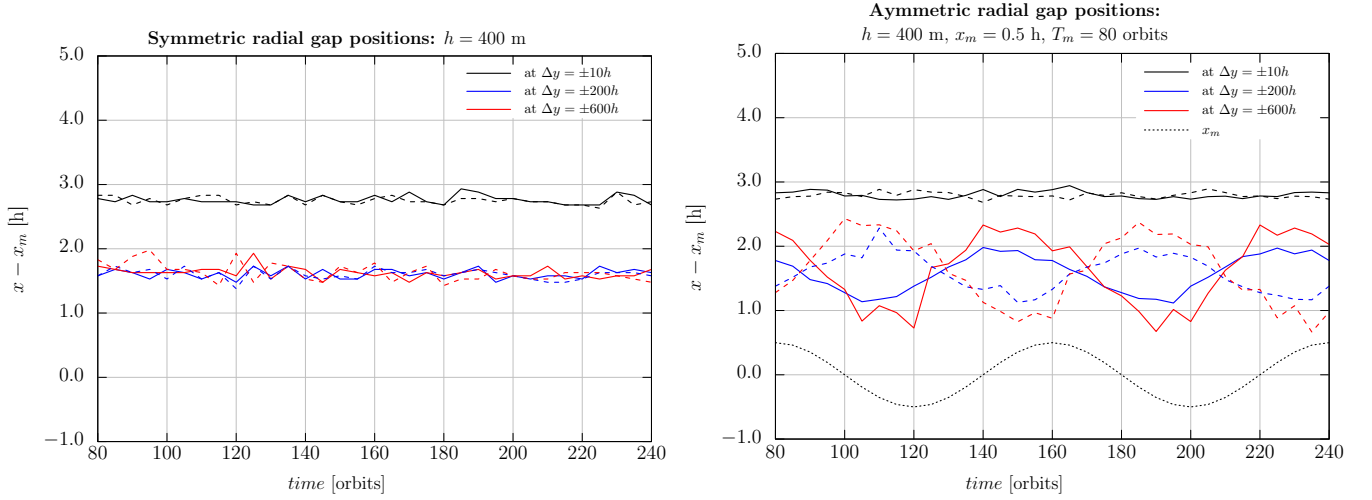


**Figure 4.** Evolution of the radial gap minima location for the symmetric (left) and asymmetric (right) propeller at azimuthal distances to the moonlet of  $\Delta y = \pm 10$  h (black),  $\pm 200$  h (blue) and  $\pm 600$  h (red). The coordinate system is moonlet-centered, meaning, that the current moonlet position  $\Delta x = x - x_m(t)$  and  $\Delta y = y - y_m(t)$  has been subtracted of. The dashed and solid lines denote the outer and inner gap profile. The moonlet's radial position in the right panel is shown by the black dotted line. An increasing radial amplitude of the changing gap minima locations can be seen for larger azimuths. For the simulation the moonlet has the Hill radius  $h = 400$  m and was librating with a period and amplitude of 80 orbits and 0.5 h.

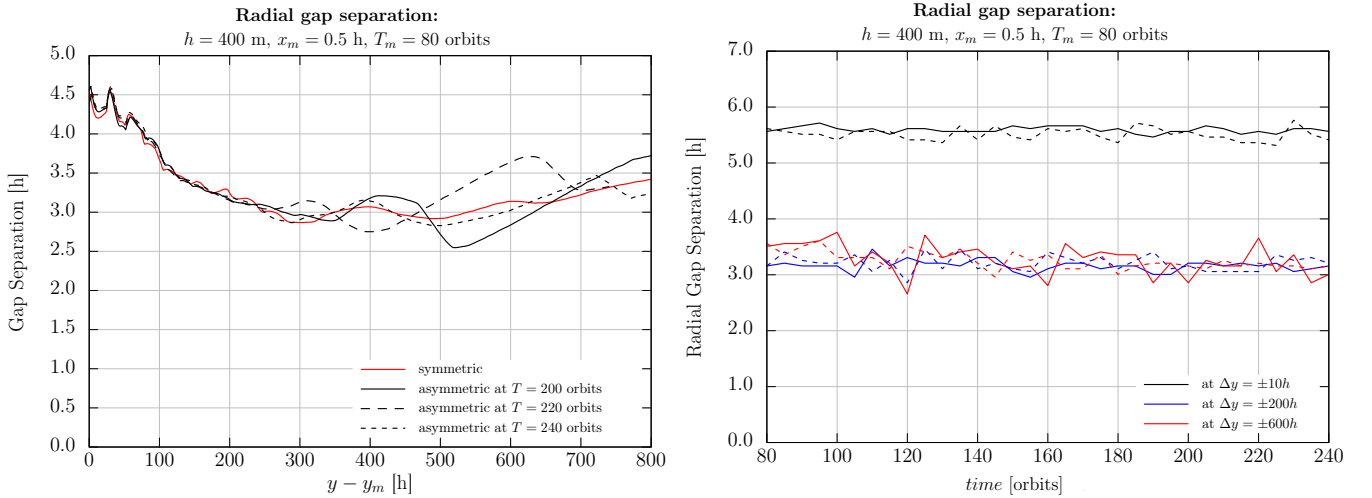


**Figure 5.** Gap Separation for a symmetric and asymmetric propeller structure for a moonlet with  $h = 400$  h Hill radius. For the asymmetric propeller structure the moonlet was librating with a period of 80 orbits and an amplitude of 0.5 h. For all realizations, a moonlet-centered reference frame has been used. Left: Radial gap separation along the azimuth. Red and black solid lines denote the symmetric and asymmetric propeller structure. The asymmetric propeller structure is presented at different snapshots at  $T = 200, 220$  and  $240$  orbits. Right: Radial gap separation for a symmetric (dashed) and asymmetric (solid) propeller structure at azimuthal distances to the moonlet of  $\Delta y = \pm 10$  h (black),  $\Delta y = \pm 200$  h (blue) and  $\Delta y = \pm 600$  h (red).

effect of the moonlet motion on the gap width by estimating the gap width at 80 % gap closing ( $\Sigma/\Sigma_0 = 0.8$ ).

The resulting gap widths for the inner and outer gap are shown in Figure 6. A concave decrease for all curves can be seen, resulting from the azimuthal gap relaxation. A similar trend holds for the gap depths.

In the panels of Figure 6 the dashed lines refer to the symmetric propeller structure, whereas the solid lines represent the widths of the asymmetric gap structures. The red and black colors denote the outer and inner gap structure. In all representations the gap widths of the symmetric and asymmetric gaps differ significantly. The moonlet libration can be identified by the intersection points of the inner and outer gap width profiles (right panel, Figure 6), where the gap widths exchange their roles.

Figure 7 shows a comparison of the time-evolution of the asymmetric  $W_a$  and symmetric  $W_s$  gap widths at two fixed azimuthal distances ( $\Delta y = \pm 200$  h and  $\Delta y = \pm 400$  h) and for the density level  $\Sigma/\Sigma_0 = 0.8$ . The left panel shows the evolution of  $W_s(t)$  for the symmetric propeller, while the right one shows  $W_a(t)$  for the asymmetric propeller. For the symmetric case, the values of  $W_s$  for the inner and outer gap fall on top of each other, while they increase in time to reach the saturation steady state which are  $\langle W_s \rangle \approx 2.7$  h for  $\Delta y = \pm 200$  h and  $\langle W_s \rangle \approx 1.9$  h for  $\Delta y = \pm 400$  h. The latter lower value is to be expected because the viscous diffusion reduces the width  $W_{s/a}(\Delta y)$  with growing azimuth  $\Delta y$ .

Quite different is the case for the librating moonlet, given in the right panel of Figure 7, where the widths  $W_a(t)$  oscillate with the libration of the moonlet and are obviously in opposite phases (anti-phase). Again, the mean values  $\langle W_a \rangle$  are smaller for the larger azimuthal cut at  $\Delta y = \pm 400$  h, while, interestingly, the amplitude of the oscillation is larger

(about  $\langle W_a(\Delta y = \pm 200 \text{ h}) \rangle = 2.76$  h against  $\langle W_a(\Delta y = \pm 400 \text{ h}) \rangle = 1.8$  h for the inner gap and  $\langle W_a(\Delta y = \pm 200 \text{ h}) \rangle = 2.63$  h against  $\langle W_a(\Delta y = \pm 400 \text{ h}) \rangle = 1.56$  h for the outer gap).

#### 3.2.4. Gap Depth

Another measurable quantity is the gap depth, given by  $d(t) = \frac{\Sigma_{min}(r) - \Sigma_0}{\Sigma_0}$ . As in the asymmetric case the gap widths  $W(t)$  and lengths  $L(t)$  are changing with time, an analogous behavior is to be expected for  $d(t)$ .

Figure 8 shows the time-evolution of  $d(t)$  for the symmetric case (left panel) and the asymmetric case (right panel) for different values of  $\Delta y$ .

While for the symmetric case (left panel) the values of  $d_s(t)$  for the outer and inner propeller wing coincide and slightly relax to the steady state, the asymmetric value of  $d_a(t)$  (right panel) oscillates with the moonlet libration, similarly to the width  $W_a(t)$ . The amplitude of this depth-variation is about  $\Delta d(t) = \frac{d_{max} - d_{min}}{\langle d \rangle} \approx 10\%$ .

### 3.3. Azimuthal Gap Relaxation

To estimate the azimuthal gap relaxation, we study the dependence of the gap minimum on the azimuthal distance to the moonlet.

In order to extract the azimuthal gap profiles, we smoothen the radial profiles with a moving box averaging method, where the box size has been set to  $\Delta x = \pm 0.5$  h. This reduces the radial scattering of the found gap minima locations especially in the wake region. Further, we use another moving box averaging process to avoid the azimuthal scattering of data due to the wakes. For this reason, we set the box size to  $\Delta y = \pm 25$  h. The resulting azimuthal gap relaxation profiles are shown in Figure 9 for the symmetric (dashed lines) and asymmetric (solid lines) propeller.

In the left and right panel the asymmetric propeller minima are presented at orbit 220 and

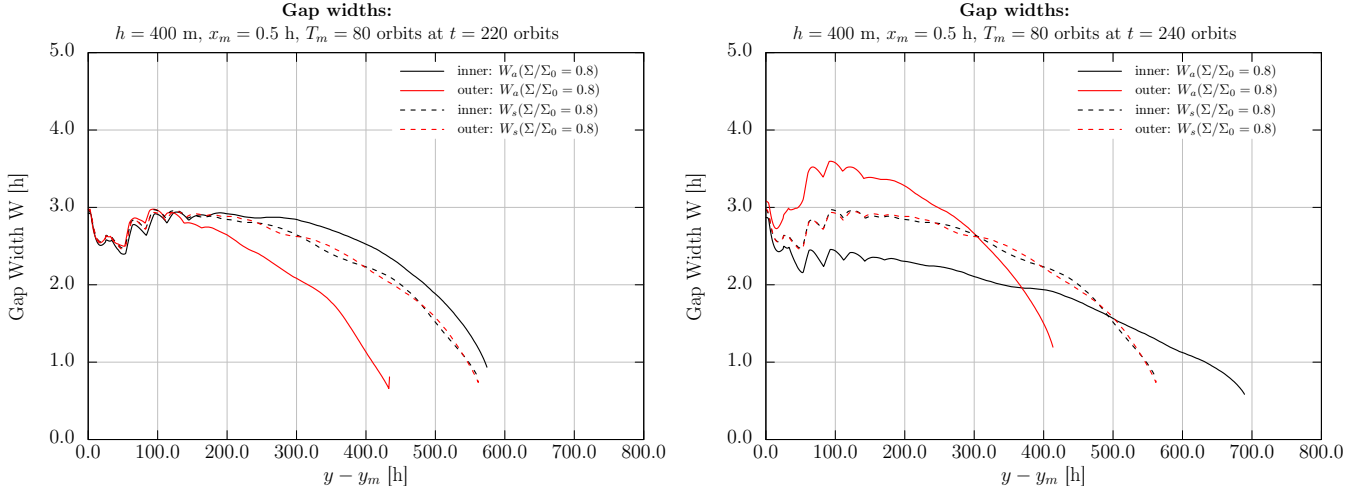


**Figure 6.** Comparison of the gap width at  $\Sigma/\Sigma_0 = 0.8$  for the symmetric (dashed) and asymmetric propeller (solid) at  $T = 220$  orbits (left) and  $T = 240$  orbits (right). The widths of the inner and outer gap are given by the black and red colored lines. The results have been obtained from simulations of a  $h = 400$  m sized moonlet, which was librating with a radial amplitude and period of 0.5 h and 80 orbits for the asymmetric case.

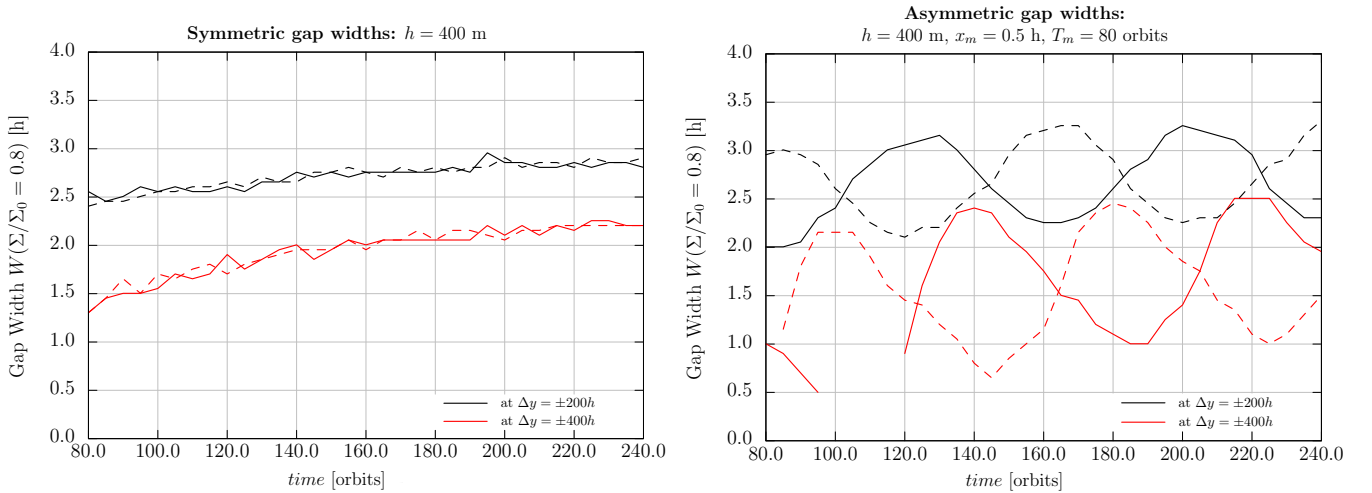


**Figure 7.** Comparison of the gap width evolution of the inner (solid) and outer (dashed) propeller gap for a non-librating (left) and librating (right) central moonlet at  $\Sigma/\Sigma_0 = 0.8$  for  $\Delta y \pm = 200$  h (black) and  $\Delta y \pm 400$  h (red). For the non-librating moonlet the values of  $W_s(t)$  fall on top of each other, giving mean values of  $\langle W_s \rangle \approx 2.7$  h for  $\Delta y = \pm 200$  h and  $\langle W_s \rangle \approx 1.9$  h for  $\Delta y = \pm 400$  h, respectively. For the librating moonlet, the gap widths oscillate with the moonlet and show an anti-phase relation. Their mean values slightly differ:  $\langle W_a(\Delta y = \pm 200 \text{ h}) \rangle = 2.76$  h against  $\langle W_a(\Delta y = \pm 400 \text{ h}) \rangle = 1.8$  h for the inner gap and  $\langle W_a(\Delta y = \pm 200 \text{ h}) \rangle = 2.63$  h against  $\langle W_a(\Delta y = \pm 400 \text{ h}) \rangle = 1.56$  h for the outer gap. Interestingly, the amplitude of the oscillation is increasing for larger azimuth.

240 of the integration time, respectively. The red and blue colors denote the outer and inner gaps. Comparing the non-librating and librating moonlet a clear difference in the gap relaxation can be observed. While for the symmetric propeller the inner and outer gaps are closing

in the same way with growing azimuth (except small variations due to the wakes and noise), the gap depths change along the azimuth for the asymmetric propeller.

Due to the retardation, the influence of changes in the moonlet's radial libration are

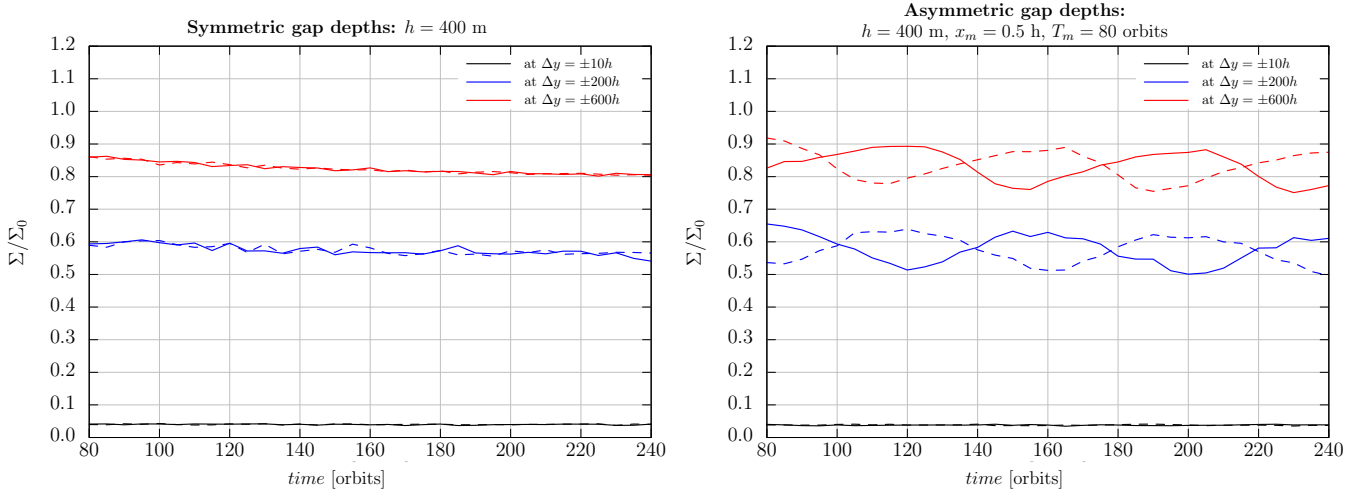


**Figure 8.** Evolution of the propeller gap depth for the symmetric (left) and asymmetric (right) propeller at different azimuthal positions to the moonlet  $\Delta y = \pm 10h$  (black),  $\Delta y = \pm 200h$  (blue) and  $\Delta y = \pm 600h$  (red). The solid and dashed lines represent the inner and outer propeller gap.

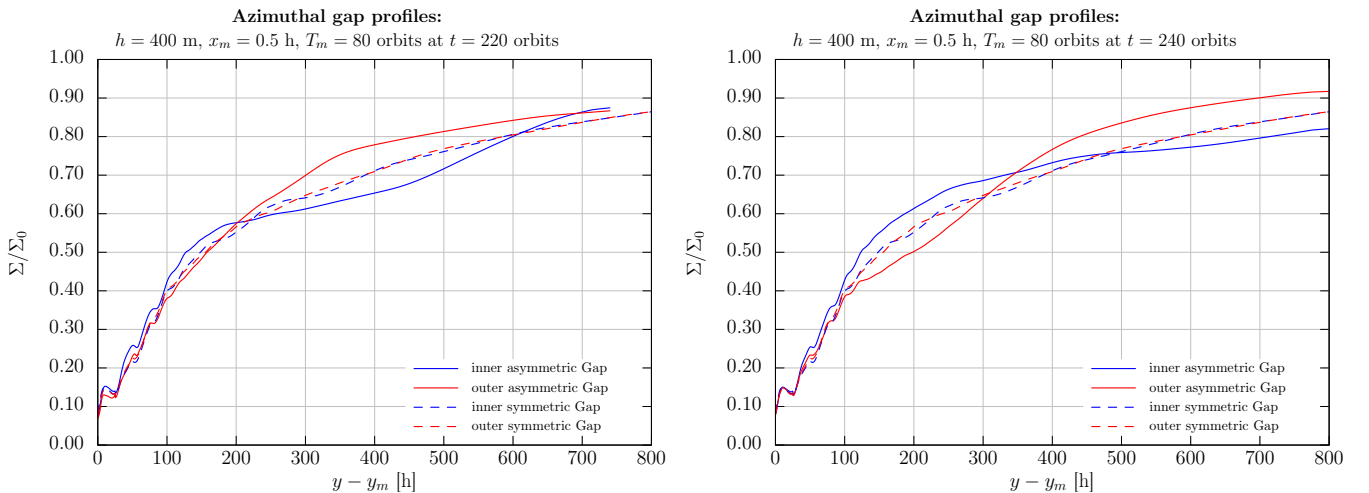


**Figure 9.** Azimuthal gap relaxation profile for the symmetric (dashed) and asymmetric (solid) gap structure at  $T = 220$  orbits (left) and  $T = 240$  orbits. Comparing the inner (blue) and outer (red) gap profiles in the symmetric case, we clearly see how both profiles match perfectly. In the asymmetric case the symmetry of the propeller is broken, which can be seen from the different lengths and the different depths of the gaps at different azimuthal distances to the moonlet.

found by the intersection points of the minima density curves (see right panel, Figure 9) for the inner and outer gap. As an example, seen in the right panel, the inner gap is closing faster than the outer one until 400 h azimuthal distance to the moonlet, respectively. There, an intersection point of both gap profile curves can be found. From this distance on, the outer gap is closing faster and stays over the density min-

ima of the inner gap. This intersection point is caused at  $T \approx 200$  orbits, where the moonlet is at its lowest radial elongation  $x_m = -0.5h$  (compare with Figure 4). At this turning point, the moonlet starts to migrate outwards again.

### 3.3.1. Gap Length

From the azimuthal gap profile we define the gap length  $L_{80}$  as the azimuthal distance to the

moonlet at  $\Sigma/\Sigma_0 = 0.8$  for the inner and outer gap structure.

The evolution of the gap length  $L_{80}(t) = L(\Sigma/\Sigma_0 = 0.8, t)$  is presented in Figure 10, where the symmetric (red color) and asymmetric (black color) propeller is presented. The dashed and solid lines denote the outer and inner gaps. The dotted line represents the azimuthal evolution of the azimuthal moonlet position as a reference. The asymmetric propeller gap length varies in phase with the moonlet motion. For the non-librating central moonlet, the mean gap length  $\langle L_{80} \rangle$  is about 539.5 h, respectively, while the for asymmetric propeller, the mean gap lengths slightly differ ( $\langle L_{80} \rangle = 511$  h for the inner gap against  $\langle L_{80} \rangle = 523$  h for the outer gap) and the maximum difference of the gap lengths is about 300 h.

Although the depths of the gaps only differ by about 10% (compare Section 3.2.4) these variations result in large azimuthal changes in the gap lengths. Thus, studying the azimuthal gap profiles is the favorable method to search for the imprint of the asymmetry.

### 3.4. The Gap Contrast

As already carried out, the azimuthal gap profiles of the inner and outer gap structures differ for a librating moonlet. In order to extract the perturbation by the moonlet motion and to study its propagation through the gaps, we define the *gap contrast* as the difference of the inner and outer gap profiles.

The retardation of the symmetry-breaking perturbation by the moonlet libration along the gap length sets a memory timescale  $T_{gap}$ . Changes in the radial moonlet motion, happening within this timescale, become visible as zero value crossings and help to differ a periodic motion from a migration in this way.

Figure 11 shows the gap contrast estimated from the azimuthal gap relaxation profiles presented in Figure 9. The red solid line repre-

sents the gap contrast of the symmetric propeller structure along increasing azimuthal distance to the moonlet. Its maximum corresponds to deviations caused by the wake region ( $\Sigma/\Sigma_0 \approx 2 \times 10^{-2}$ ) and thus defines the level, where the symmetric and asymmetric propeller will not be distinguishable anymore. The black lines in Figure 11 represent the gap contrast for the asymmetric gap structure at different integration times, where the solid, dashed and dotted lines show the gap contrast at  $T = 200, 220$  and 240 orbits. The different snapshots for the asymmetric propeller demonstrate, how the perturbation by the moonlet libration propagates through the gaps. As an example, the minimum at  $T = 200$  orbits shifts from  $\Delta y = 200$  h and  $\Sigma/\Sigma_0 = -0.1$  to  $\Delta y = 400$  h and  $\Sigma/\Sigma_0 = -0.12$  at orbit 220 and further to  $\Delta y = 650$  h and  $\Sigma/\Sigma_0 = -0.1$  at orbit 240. The transport of perturbations along the azimuth resembles a propagating wave package. Like a dissipating wave package, the perturbation gets smeared along the azimuth due to diffusive effects.

## 4. RING - MOONLET INTERACTIONS

The symmetry breaking of the propeller structure disturbs the force balance of the gravity by the ring ensemble reacting on the moonlet Seiler et al. (2017). Here, we calculate the resulting force of the surrounding ring material on the moonlet. Therefore, we calculate the gravity of every grid cell onto the moonlet and sum over all the contributing cells of the grid. We exclude a circular area  $r = [(x - x_m)^2 + (y - y_m)^2]^{1/2} = 1.2$  h around the moonlet from the force calculation in order to account for the physical dimension of the moonlet, which is treated as a point mass in our simulations. The resulting total gravitational interaction between the ring and the moonlet  $F_x$  and  $F_y$  in radial and azimuthal direction is given by the sum of the contributing cells



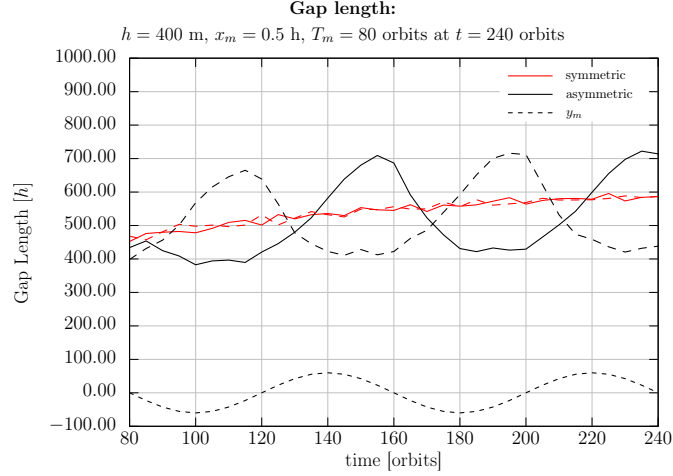


**Figure 10.** Comparison of the gap length at 80% relaxation for the symmetric (red) and asymmetric propeller (black). The length of the inner and outer gap are given by the solid and dashed lines. The results have been obtained from the simulation of a  $h = 400 \text{ m}$  sized moonlet. For the asymmetric propeller the moonlet was librating with a radial amplitude of  $0.5 \text{ h}$  and period of 80 orbits. For comparison the azimuthal evolution of the librating moonlet is plotted as the black dotted line as well. For both profile plots a moonlet-centered reference frame has been chosen for better comparison.

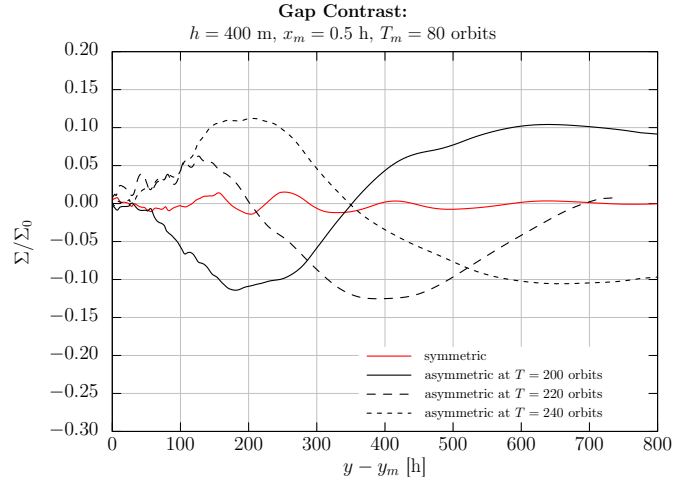


**Figure 11.** Difference of the azimuthal gap relaxation of the inner and outer gap (*gap contrast*) for a non-librating (red) and librating (black) central moonlet of size  $r_h = 400 \text{ m}$  at orbits 200, 220 and 240 (solid, dashed and dotted).

$$F_x(x, y, x_m, y_m) = -G\Delta A \sum_{\text{Grid}} \Delta\Sigma_i \frac{x_m - x_i}{|\vec{r}_m - \vec{r}_i|^3} \quad (14)$$

$$F_y(x, y, x_m, y_m) = -G\Delta A \sum_{\text{Grid}} \Delta\Sigma_i \frac{y_m - y_i}{|\vec{r}_m - \vec{r}_i|^3}, \quad (15)$$

with  $\vec{r}_i = (x_i, y_i)$  and  $\vec{r}_m = (x_m, y_m)$  the position vectors of the  $i$ -th cell and the moon-

let. The quantities  $\Delta\Sigma_i = \Sigma_i - \Sigma_0$  and  $\Delta A = \Delta x_i \times \Delta y_i$  denote the difference in the surface mass density with respect to the initial one and the surface of the equal-sized grid cells.

The left panel in Figure 12 illustrates the evolution of the normalized ring gravity, where the  $x$  (red) and  $y$  (blue) component of the ring gravity are following the moonlet motion ( $x_m$  and  $y_m$  are represented by the dashed and solid black

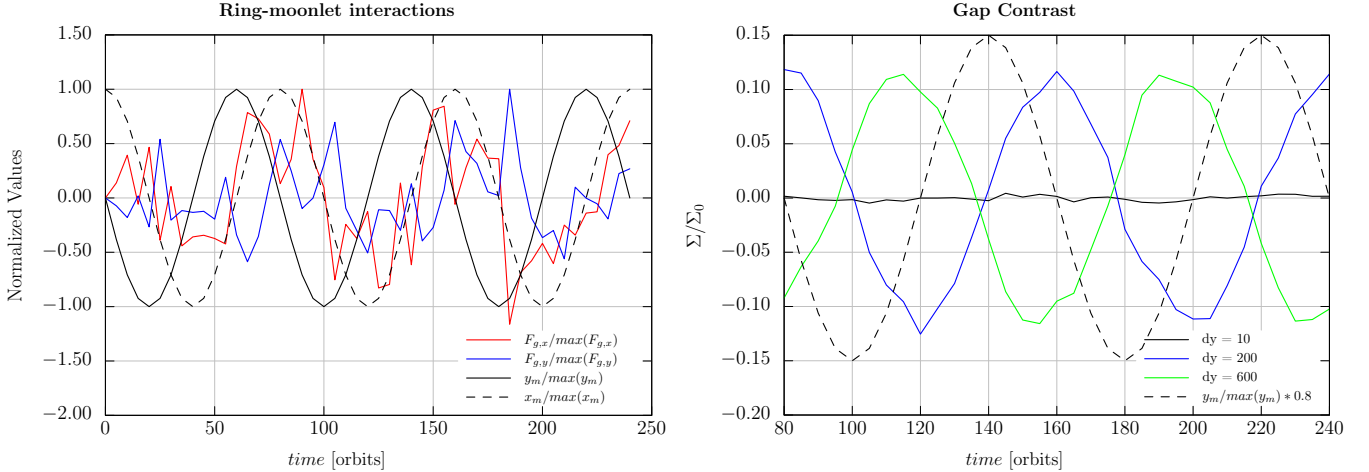


**Figure 12.** Left: Time evolution of the normalized moonlet motion in x (black dashed line) and y (black solid line) direction and the x (blue) and y (red) component of the ring gravity acting on the moonlet. Right: Evolution of the gap contrast at different azimuthal positions, illustrating, how the variation of the gap contrast is following the moonlet motion (black dashed line).

lines). The right panel shows a comparison of the gap contrast evolution and the moonlet evolution, where the gap contrast is presented at three different azimuthal distances to the moonlet. The evolution for  $\Delta y = \pm 200$  h and  $\delta y = \pm 600$  h displays the retardation set by the Kepler shear and the decreasing amplitude of the gap contrast with increasing azimuths. The force and the maximum contrast are following the moonlet motion with a slight delay (*phase shift*).

## 5. SYSTEMATIC ASYMMETRY PREDICTIONS

In this section we test the dependence of the propeller’s asymmetry on the *a)* the libration amplitude and *b)* the libration period. This allows us to make predictions for the observability of the asymmetry of propeller gap structures in Saturn’s rings. Therefore, at first, we keep the libration period constant at  $T_m = 80$  orbits and vary the initial radial amplitude  $x_{m,0}$ . In a second analysis, we perform simulations, where the initial radial amplitude  $x_{m,0} = 1$  h will be kept constant, while the libration period is varied. For both scenarios we will study the gap contrast, the gap length and width at  $\Sigma/\Sigma_0 = 0.8$ .

Note, that our analysis does not consider any resonances in the vicinity of the propeller structure, which might have an additional effect of the final asymmetry for larger radial amplitudes and libration periods.

For each simulation parameter, at each time the above quantities will be determined. Further, the mean value, the maximum and minimum at each time will be estimated along the azimuth. Finally, for the complete simulation time frame the global maximum, minimum and mean values will be calculated. The resulting values will be presented in the following sections.

### 5.1. Dependence of Asymmetry on the Libration Amplitude

We vary the libration amplitude  $x_{m,0}$  from 0.125 h through 4 h.

In Figure 13 the dependence of the maximum gap contrast from the radial amplitude of the moonlet libration is shown. Here, we can fit the data by the exponential relation

$$C(x_m) = C_0 - C_{max} \exp[-\lambda x_m], \quad (16)$$

with  $C_{i,0} = 0.925$ ,  $C_{i,max} = 0.971$  and  $\lambda_i = 0.458 \text{ h}^{-1}$  for the maximum  $C_{o,0} = 0.923$ ,

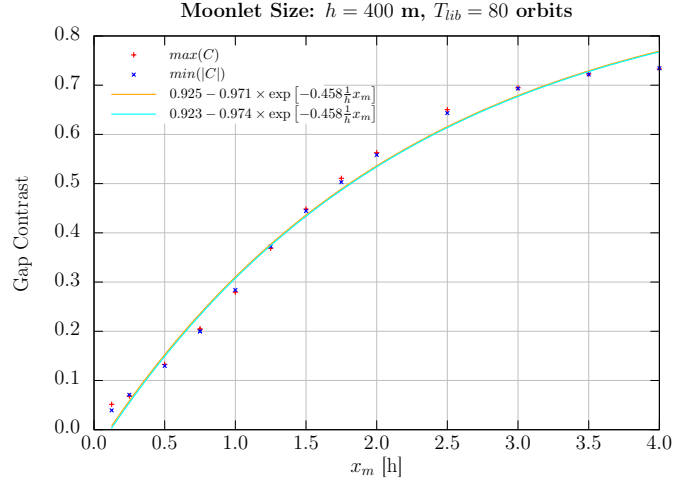


**Figure 13.** Dependence of the maximal asymmetry from the moonlet’s libration amplitude for constant libration period  $T_m = 80$  orbits.

$C_{o,max} = 0.974$  and  $\lambda_o = 0.458 \text{ h}^{-1}$  for the minimum gap contrast.

Starting from small amplitudes the contrast is increasing for growing initial amplitude until the saturation of about  $C = 0.925$  is reached. From this amplitude on the gap contrast is not increasing anymore. For amplitudes larger  $x_{m,0} = 1.6 \text{ h}$  the moonlet starts to migrate through its created gaps, and thus, destroys its own propeller structure, explaining the maximum saturation level.

Figure 14 illustrates the dependence of the gap length  $L_{80}$  (left panel) and the gap width  $W_a$  (right panel) on the libration amplitude. For the gap length, a clear drop in the mean gap length can be noticed for larger amplitudes, while the maximum difference in the gap lengths of the inner and outer gap first increases from 200 h to 500 h for  $x_{m,0} = 0.125 \text{ h}$  to  $x_{m,0} = 1 \text{ h}$  and then reduces to about 200 h. With the gap length the gap width changes as well (see right panel of Figure 14), but here, the mean gap width is increasing from 2.25 h to 2.6 h for larger amplitudes, until at about  $x_{m,0} = 1.6 \text{ h}$  a saturation level is reached. A similar result can be seen for the maximum difference of the inner and outer gap width, which increases from 0.5 h to 3.5 h, respectively.

To summarize, with larger radial amplitudes the perturbation by the moonlet motion increases, which results in shorter gap lengths, broader gaps and larger gap contrast until the perturbation exceeds a critical level, where the creation of the propeller structure is prevented.

## 5.2. Dependence of Asymmetry on the Libration Period

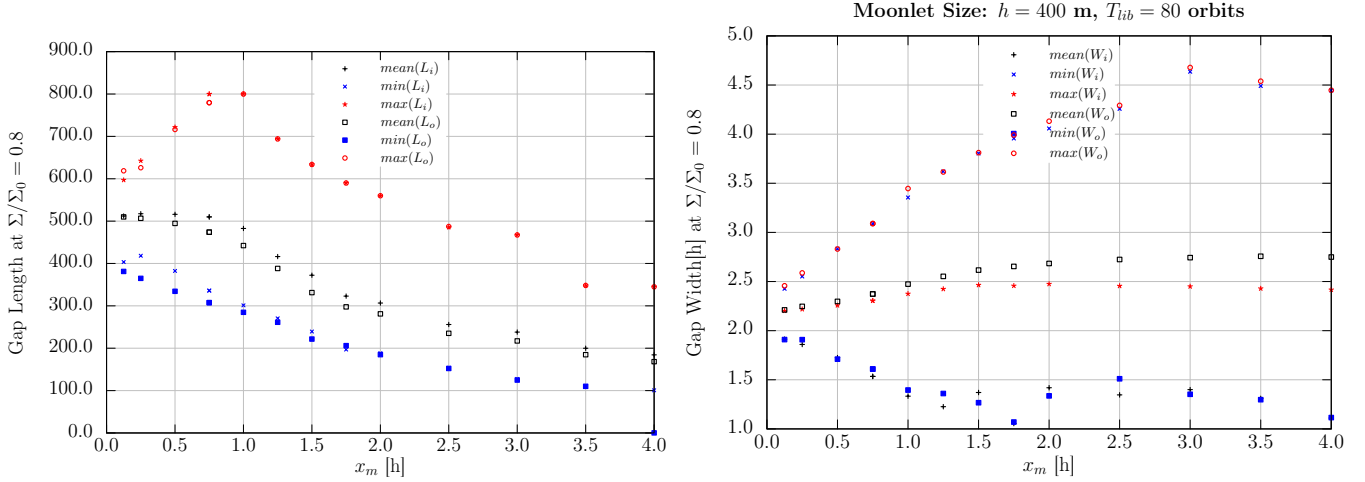
We vary the libration period of the moonlet from  $T_m = 15$  orbits to  $T_m = 320$  orbits, while we keep the radial amplitude fixed at  $x_{m,0} = 1 \text{ h}$ .

Figure 15 shows the dependence of the gap contrast on the libration period, where an exponential relation given by

$$C(T_{lib}) = C_0 + C_{max} \exp[-\lambda T_{lib}], \quad (17)$$

with  $C_0 = 0.125$ ,  $C_{max} = 0.587$  and  $\lambda = 0.013 \text{ orbit}^{-1}$  can be found.

For fixed radial amplitude the changes for larger libration periods result in a growing azimuthal excursion of the moonlet (see Eq. 11). As the libration period grows, the relative velocity to the unperturbed orbit decreases and thus the perturbation by the changing moonlet position can be easily transported to larger azimuthal distances, resulting in a more symmet-



**Figure 14.** Dependency of the gap length (left) and gap width (right) at  $\Sigma/\Sigma_0 = 0.8$  from the moonlet’s libration amplitude for the inner and outer gap.

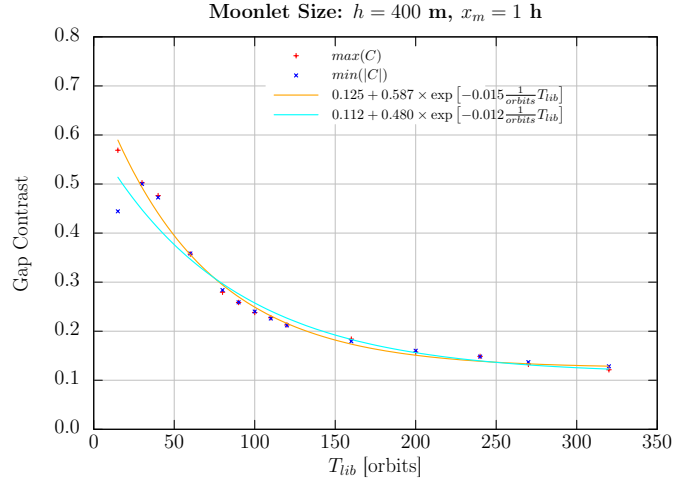


**Figure 15.** Dependence of the maximal asymmetry on the moonlet’s libration period for constant radial amplitude  $x_{m,0} = 1 \text{ h}$ .

ric propeller structure and therefore in a lower gap contrast (see Figure 15).

In Figure 16 the dependence of the gap length (left panel) and the gap width (right panel) on the libration period is presented.

The gap length (left panel) first increases from 350 h to about 500 h with respect to the libration period interval from  $T_0 = 15$  orbits through  $T_0 = 80$  orbits. For this interval, the maximum difference in the gap lengths between outer and inner gap increase from 400 h to about 600 h. At  $T_m = 80 \text{ h}$  the gap passage time equals the libration period of the moonlet allowing the per-

fect transport of the perturbation through the gaps. At this optimal parameter set the gap width reaches its maximum of about 2.5 h, respectively, while the differences in the gap width between inner and outer gap are at their maximum of about 2 h (compare right panel). For increasing libration periods, the relative velocity of the moonlet to its unperturbed orbit decreases, resulting in smaller perturbations and therefore in a more symmetric propeller structure. For this reason, the mean gap length drops to about 500 h – close to the value of the unperturbed propeller gap length. Further, the

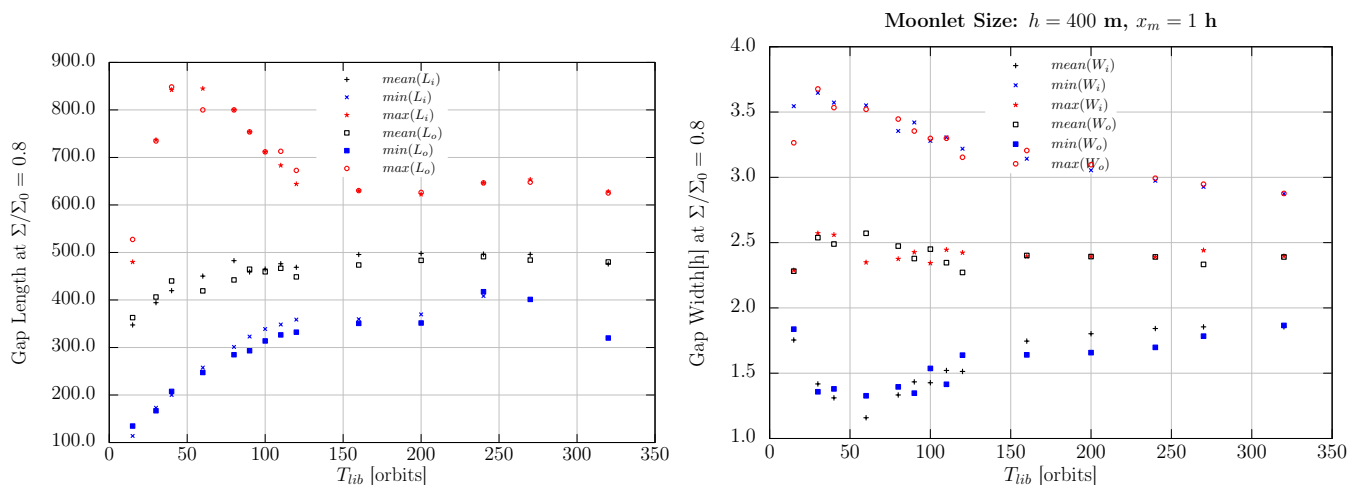


**Figure 16.** Dependence of the gap length (left) and gap width (right) at 80% gap relaxation from the moonlet’s libration amplitude for fixed radial amplitude  $x_{m,0} = 1$  h.

maximum difference in the gap length drops to an almost constant level of 200 h as well. Exceeding a libration period of  $T_m = 80$  orbits the mean gap width stays almost constant at 2.5 h, which is very close to the unperturbed value of 2.6 h. Nevertheless, the moonlet motion still induces a difference of the gap widths of about 1 h.

To summarize, for small libration periods ( $T_m \leq T_{gap}$ ) the asymmetry is large because of the strong perturbation by the moonlet motion and the retardation, while for large periods ( $T_m > T_{gap}$ ) the asymmetry gets smaller due to quasi-static changes in the moonlet motion. However, the asymmetry is still measurable but depends on the actual libration phase angle of the moonlet at the observation time.

### 5.3. Application to the Propeller Blériot

The excess motion of Blériot has been reconstructed by three overlaying harmonic functions, where we assume the moonlet to librate with the largest amplitude and period of about 1845 km and 11.1 years (see e.g. Seiler et al. 2017; Spahn et al. 2018). Translating the fitted period to number of orbits results  $T_m =$

11.1 years = 6941 orbits and thus, the radial amplitude for the moonlet is given by

$$|\delta x| = \frac{2 \Delta y}{3 \Omega t} = \frac{2 \cdot 1845 \text{ km}}{3 \cdot 6941 \text{ orbits}} = 0.177 \text{ km} \quad (18)$$

This agrees with the radial amplitude estimated from orbital fits by Spahn et al. (2018), who estimated the radial deviation to be about 200 m. The Hill radius of Blériot is about  $r_H = 450$  m (Hoffmann et al. 2016; Seiler et al. 2017) and thus, the estimated radial amplitude corresponds to  $x_{m,0} \approx 0.4$  h.

For Blériot Seiler et al. (2017) estimated  $T_{gap} \approx 0.5$  years which corresponds to 313 orbits, respectively. Thus, for Blériot we need to consider the case  $T_m = 11.1$  years = 6941 orbits  $\gg$  313 orbits = 0.5 years =  $T_{gap}$ . At this ratio the gap contrast is already at its lowest level of about 0.125 in comparison to the noise level of the unperturbed propeller gap contrast of 0.02.

The maximum gap contrast illustrated Figure 13 can be linearly approximated in the range  $x_{m,0} = [0, 1.5 \text{ h}]$ . Therefore, the expected gap contrast level of about  $C_0 = 0.125$  estimated for  $x_{m,0} = 1$  h (see Figure 15) can be interpolated to  $x_{m,0} = 0.5$  h, yielding 0.063, respectively. Following this interpolation, the maximum variation in gap length and gap width are expected to be about 125 h and 0.5 h, respectively.

## 6. CONCLUSION AND DISCUSSION

In this work, we have studied the formation of asymmetric propeller structures in Saturn's A ring, assuming a libration of the moonlet. Note, that in this work, we did not consider the reason for the moonlet libration, which we simply considered as given. In practice, librational behavior sensitively depends on the perturbation forces and sources (e.g. resonances, density fluctuations, particle collisions). It turned out, that the additional moonlet motion is perturbing the induced propeller structure, causing an asymmetry in this way. The perturbation by the moonlet motion gets transported through the gaps with the Kepler speed and thus arrives at the gap ends after a delay time  $T_{gap}$ . This retardation depends on the gap length and sets a memory time, which finally causes the asymmetric appearance of the propeller structure in the images. The main implications of our simulations are:

### 6.1. Timescales vs Asymmetry

We studied the dependence of the asymmetry on the libration period and amplitude. Three general cases have been investigated:

- i)  $T_m < T_{gap}$  : For small libration periods the asymmetry is large. This results from the strong perturbation by the moonlet motion, which causes large variations in all gap properties, which even can prevent the propeller formation. Thus, small libration periods are similar to the scenario of large libration amplitudes.
- ii)  $T_m = T_{gap}$  : The strongest asymmetry has been identified, if the libration period matches the gap timescale. In this case, the perturbation by the moonlet motion gets transported in the most effective way ( in a kind synchronized way), resulting in the largest variations in the gap length and width.

- iii)  $T_m > T_{gap}$  : The quasi-static changes in the moonlet motion result in a less asymmetric shape of the propeller. Thus, the gap contrast is minimal and the variations in the gap width and gap length are rather small.

### 6.2. Libration vs. Migration

The retardation limits the observability of the asymmetry and with it the chance to distinguish a migration of the moonlet from a libration. Changes in the direction of the moonlet motion (inward and outward movement) result in zero value crossings in the gap contrast along the azimuth. Depending on the libration period, three limiting cases can be distinguished:

- i)  $T_m < T_{gap}$  : The frequent changes in the moonlet motion can be seen due to the retardation, resulting in at minimum two intersection points in the gap profile (or zero values crossings for the gap contrast, respectively). Thus, the periodicity of the moonlet motion is well reflected by the propeller.
- ii)  $T_m = T_{gap}$  : At maximum two (at minimum one) intersection points in the azimuthal gap profile can be identified, depending on the libration phase of the moonlet at the observation time.
- iii)  $T_m > T_{gap}$  : The slow outward and inward migration of the moonlet results in at maximum one (minimum zero) observable intersection points.

In order to identify a librational motion of the moonlet, the libration period needs to be smaller than the memory time  $T_m < T_{gap}$ . For larger libration periods the gap contrast will only change its sign at the turning points of the radial moonlet libration. In between no change in sign will be visible and therefore the moonlet libration might be misinterpreted as a radial drift.

### 6.3. Observability of the Asymmetry

In order to measure the asymmetry of the propeller structure, our analysis has shown, that the azimuthal profiles are the most favorable to consider for processing Cassini ISS images. Especially for larger azimuthal distances to the moonlet ( $\Delta y > \pm 100$  h), already small changes in the gap minima can result in large differences in the gap lengths.

However, in case of high-resolution images, such as UVIS scans, small variations in the radial gap profile can be resolved, allowing to study the asymmetry even in those profiles.

Nevertheless, in all cases both, inner and outer gap, need to be recorded.

### 6.4. Asymmetry of the Propeller Blériot

Our predictions yield, that an asymmetry in the gap contrast should be visible by about 6.3%, which still is larger than the noise level for the unperturbed propeller. The gap width differences comparing inner and outer gap structure should be about 0.5 h and the gap lengths are expected to differ by 125 h. These variations should be still detectable, but depend on the libration phase of the central moonlet at the time of observation.

Due to the large libration period of Blériot at maximum one zero value crossing for the gap contrast can be expected, which makes it impossible to judge whether the moonlet is librating or migrating considering one single observation. An analysis of several images of Blériot at different times would be necessary to search for moving patterns (changes in the sign and amplitudes) in the gap contrast along the azimuth.

### 6.5. Asymmetry of other Propellers

Although the asymmetry for Blériot might be rather small, the asymmetry for the other giant trans-Encke propellers might be easier to detect. As an example, the propeller structures Earhart and Santos Dumont are smaller

than Blériot but show similar residual amplitudes (Tiscareno et al. 2010; Spahn et al. 2018), resulting in larger radial amplitudes for an assumed moonlet libration. Further, due to the smaller size of these moonlets, their induced propeller wings' azimuthal extent is smaller by  $M_m/\nu_0 \propto h^3/\nu_0 \propto L/\nu_0$  (Spahn and Sremčević 2000), allowing to record both propeller wings at the same time with one observation.

### 6.6. Propeller-Moonlet Interactions

The formation of an asymmetric propeller structure due to the motion of the moonlet causes a non-balancing force of the ring material on the moonlet. Calculating the force of the ring material on the moonlet we find, that it is dominated by the azimuthal amplitude of the moonlet (Seiler et al. 2017) and follows the moonlet motion with a phase shift according to the Kepler shear. Thus, our simulations agree with the simple propeller-moonlet interaction model suggested by Seiler et al. (2017).

### 6.7. Outlook

Although the implementation of a librating moonlet is a simplification, our simulation however gives an insight of how the propeller structure reacts to perturbations and how the resulting asymmetry will look like. Further, our simulations have shown, that the retardation along the azimuth is the main mechanism to make the asymmetry measurable in the images. Therefore, even for an underlying stochastic migration of the central moonlet, an asymmetry might form. The observability of the resulting asymmetry then will depend on the collision frequency and the memory time of the gap.

However, in order to build a fully consistent model, as a next step, the moonlet needs to be simulated in a box where it is allowed to move freely. In this way, a stochastic moonlet motion can be simulated as well, which can be directly compared to the unperturbed and librating moonlet.

Further, allowing the moonlet to move freely within the simulation box will show, whether the back-reaction of the ring material is able to conserve an initial libration of the moonlet, which will be the final consistency test for the suggested propeller-moonlet interaction model.

Our introduction of the gap contrast allows to directly observe the propagation of the perturbation by the moonlet motion along increasing azimuth. It turned out that the perturbation by the moonlet's motion appears and behaves like a moving wave package which gets smeared along the azimuth due to the damping by the ring material. This permits to study the dispersion relation of the perturbation and further to

estimate the viscosity of the surrounding ring material from the images.

Our simulation code uses an isothermal model for the ring environment. This might result in larger viscosity values in the close vicinity of the moonlet. For a consistent model, the temperature needs to be considered in the simulations as well by including the energy equation. This might have an additional effect on the observability of the asymmetry.

This work has been supported by the Deutsche Forschungsgemeinschaft (Sp 384/28-1,2, Ho 5720/1-1) and the Deutsches Zentrum für Luft- und Raumfahrt (OH 1401).

## REFERENCES

- Bromley, B. C., Kenyon, S. J., Feb. 2013. Migration of Small Moons in Saturn's Rings. *ApJ*764, 192.
- Cooper, N. J., Renner, S., Murray, C. D., Evans, M. W., Jan. 2015. Saturn#700s Inner Satellites: Orbits, Masses, and the Chaotic Motion of Atlas from New Cassini Imaging Observations. *AJ*149, 27.
- Crida, A., Papaloizou, J. C. B., Rein, H., Charnoz, S., Salmon, J., Oct. 2010. Migration of a Moonlet in a Ring of Solid Particles: Theory and Application to Saturn's Propellers. *AJ*140, 944–953.
- Cuzzi, J. N., Filacchione, G., Marouf, E. A., 2018. The rings of saturn. In: Tiscareno, M. S., Murray, C. M. (Eds.), *Planetary Ring Systems*. "Cambridge University Press".
- Goldreich, P., 1965. An explanation of the frequent occurrence of commensurable mean motions in the solar system. *MNRAS*130, 159.
- Goldreich, P., Rappaport, N., Apr. 2003a. Chaotic motions of prometheus and pandora. *Icarus*162, 391–399.
- Goldreich, P., Rappaport, N., Dec. 2003b. Origin of chaos in the Prometheus-Pandora system. *Icarus*166, 320–327.
- Henon, M., Sep. 1981. A simple model of Saturn's rings. *Nature*293, 33–35.
- Hill, G., 1878. Researches in the lunar theory. *Am. J. Math.* 1, 5–26.
- Hoffmann, H., Chen, C., Seiß, M., Albers, N., Spahn, F., Nic, Oct. 2016. Analyzing Bleriot's propeller gaps in Cassini NAC images. In: *AAS/Division for Planetary Sciences Meeting Abstracts*. Vol. 48 of *AAS/Division for Planetary Sciences Meeting Abstracts*.
- Hoffmann, H., Seiß, M., Salo, H., Spahn, F., May 2015. Vertical structures induced by embedded moonlets in Saturn's rings. *Icarus*252, 400–414.
- LeVeque, R. J., 2002. *Finite Volume Methods for Hyperbolic Problems*. Cambridge Texts in Applied Mathematics. Cambridge University Press.
- Lissauer, J. J., Shu, F. H., Cuzzi, J. N., Aug. 1981. Moonlets in Saturn's rings. *Nature*292, 707–711.
- Pan, M., Chiang, E., Oct. 2010. The Propeller and the Frog. *ApJL*722, L178–L182.
- Pan, M., Chiang, E., Jan. 2012. Care and Feeding of Frogs. *AJ*143, 9.
- Pan, M., Rein, H., Chiang, E., Evans, S. N., Dec. 2012. Stochastic flights of propellers. *MNRAS*427, 2788–2796.



- Porco, C. C., Baker, E., Barbara, J., Beurle, K., Brahic, A., Burns, J. A., Charnoz, S., Cooper, N., Dawson, D. D., Del Genio, A. D., Denk, T., Dones, L., Dyudina, U., Evans, M. W., Giese, B., Grazier, K., Helfenstein, P., Ingersoll, A. P., Jacobson, R. A., Johnson, T. V., McEwen, A., Murray, C. D., Neukum, G., Owen, W. M., Perry, J., Roatsch, T., Spitale, J., Squyres, S., Thomas, P., Tiscareno, M., Turtle, E., Vasavada, A. R., Veverka, J., Wagner, R., West, R., Feb. 2005. Cassini Imaging Science: Initial Results on Saturn's Rings and Small Satellites. *Science* 307, 1226–1236.
- Rein, H., Papaloizou, J. C. B., Dec. 2010. Stochastic orbital migration of small bodies in Saturn's rings. *A&A*524, A22.
- Seiler, M., Sremčević, M., Seiß, M., Hoffmann, H., Spahn, F., May 2017. A Librational Model for the Propeller Blériot in the Saturnian Ring System. *ApJL*840, L16.
- Seiß, M., Albers, N., Sremcevic, M., Schmidt, J., Salo, H., Seiler, M., Hoffmann, H., Spahn, F., Jan. 2017. Hydrodynamic simulations of moonlet induced propellers in Saturn's rings: Application to Blériot. *ArXiv e-prints* .
- Seiß, M., Spahn, F., Sremčević, M., Salo, H., Jun. 2005. Structures induced by small moonlets in Saturn's rings: Implications for the Cassini Mission. *Geophys. Res. Lett.*321, L11205.
- Showalter, M. R., Jun. 1991. Visual detection of 1981S13, Saturn's eighteenth satellite, and its role in the Encke gap. *Nature*351, 709–713.
- Spahn, F., Hoffmann, H., Rein, H., Seiß, M., Sremčević, M., Tiscareno, M. S., 2018. Moonlets in dense planetary rings. In: Tiscareno, M. S., Murray, C. M. (Eds.), *Planetary Ring Systems*. "Cambridge University Press".
- Spahn, F., Schmidt, J., Mar. 2006. Planetary science: Saturn's bared mini-moons. *Nature*440, 614–615.
- Spahn, F., Schmidt, J., Petzschmann, O., Salo, H., Jun. 2000. Note: Stability analysis of a Keplerian disk of granular grains: Influence of thermal diffusion. *Icarus* 145, 657–660.
- Spahn, F., Sremčević, M., Jun. 2000. Density patterns induced by small moonlets in Saturn's rings? *A&A*358, 368–372.
- Spitale, J. N., Jacobson, R. A., Porco, C. C., Owen, Jr., W. M., Aug. 2006. The Orbits of Saturn's Small Satellites Derived from Combined Historic and Cassini Imaging Observations. *AJ*132, 692–710.
- Sremčević, M., Schmidt, J., Salo, H., Seiß, M., Spahn, F., Albers, N., Oct. 2007. A belt of moonlets in Saturn's A ring. *Nature*449, 1019–1021.
- Sremčević, M., Spahn, F., Duschl, W. J., Dec. 2002. Density structures in perturbed thin cold discs. *MNRAS*337, 1139–1152.
- Tiscareno, M. S., Mar. 2013. A modified "Type I migration" model for propeller moons in Saturn's rings. *Planet. Space Sci.*77, 136–142.
- Tiscareno, M. S., Burns, J. A., Hedman, M. M., Porco, C. C., Mar. 2008. The Population of Propellers in Saturn's A Ring. *AJ*135, 1083–1091.
- Tiscareno, M. S., Burns, J. A., Hedman, M. M., Porco, C. C., Weiss, J. W., Dones, L., Richardson, D. C., Murray, C. D., Mar. 2006. 100-metre-diameter moonlets in Saturn's A ring from observations of "propeller" structures. *Nature*440, 648–650.
- Tiscareno, M. S., Burns, J. A., Sremčević, M., Beurle, K., Hedman, M. M., Cooper, N. J., Milano, A. J., Evans, M. W., Porco, C. C., Spitale, J. N., Weiss, J. W., Aug. 2010. Physical Characteristics and Non-Keplerian Orbital Motion of "Propeller" Moons Embedded in Saturn's Rings. *ApJL*718, L92–L96.